Indian Journal of Engineering & Materials Sciences
Vol. 33, February 2026, pp. 60-67
DOI: 10.56042/ijems.v33i01.19699

Design and optimization of high-performance organic solar cells based on DPPEZnP-TBO active layer

Sanjay Narayan Barman & Pinaki Laha*
University Department of Physics, Babasaheb Bhimrao Ambedkar Bihar University, Muzaffarpur 842 001, Bihar, India

Received: 14 May 2025; accepted: 08 December 2026

We have reported the design and simulation of an advanced multilayer organic photovoltaic (OPV) cell structure incorporating Di-(phenyl phosphoryl)-ethyl zinc porphyrin-thiophene benzothiadiazole (DPPEZnP-TBO), which has been used as an organic active layer in solar cells. DPPEZnP-TBO has exhibited exceptional light absorption and charge-transport properties. The integration of this material into solar cell architecture has significantly enhanced key performance metrics, including short-circuit current density (J_{SC}), open-circuit voltage (V_{OC}), fill factor (FF), and power conversion efficiency (PCE), resulting in substantial overall performance improvements. The influence of factors such as active-layer thickness, operating temperature, and series resistance (R_S) on the solar cell's performance has been systematically analysed to determine optimal conditions. At 325 K, the device has exhibited a V_{OC} of 1.11 V, a J_{SC} of −2.59 mA/cm², an FF of 79%, and a PCE of 2.32%. With a 40 nm front sub-cell active-layer thickness, the V_{OC} has increased to 1.12 V, J_{SC} has improved to −2.74 mA/cm², and the PCE has reached 2.44%. The FF has remained at 79%. With a series resistance of 500 Ω, the V_{OC} has remained at 1.12 V, J_{SC} at −2.59 mA/cm², FF at 79%, and PCE at 2.28%. The results have indicated promising approaches to enhancing the efficiency of bulk heterojunction solar cells.

Keywords: Deep absorbing porphyrins, DPPEZnP-TBO, Fill factor, Organic solar cells, Power conversion efficiency

1 Introduction

Organic solar cells (OSCs) have garnered significant attention due to their potential advantages, including low cost, lightweight construction, and the ability to be fabricated on flexible substrates[1-3]. The power conversion efficiency of organic photovoltaics has been increasing speedily beyond 20%[4]. This efficiency can be further enhanced using the tandem solar cell concept, which involves stacking two absorber materials with different band gaps to utilise the solar spectrum[5,6.] However, these efficiencies remain considerably lower than those of inorganic solar cells, posing challenges for large-scale practical applications. A critical factor influencing the overall performance of OSCs is the efficiency of charge extraction at the interfaces between electrodes and organic layers, as well as carrier transport within bulk organic materials[7, 8]. The power conversion efficiency (PCE) of organic solar cells (OSCs) can be enhanced by employing a tandem architecture composed of two sub-cells. This approach expands the solar spectrum's coverage while reducing photon energy losses caused by thermalisation[5,9]. To achieve optimal performance, the sub-cells must possess complementary absorption profiles and produce well-balanced, high currents[10]. Achieving these criteria requires precise design and thoughtful selection of active materials. In tandem OSCs, the active layer consists of one donor (D) material and one acceptor (A) material. The operation involves four steps. Initially, light absorption creates excitons, which are bound electron-hole pairs. These excitons then diffuse toward the donor-acceptor interface. These charges are transported with holes moving to the anode through the donor and electrons to the cathode through the acceptor[11]. Therefore, a high-performance tandem cell requires sub-cells with complementary absorption properties, high currents, demanding meticulous design and careful selection of suitable active materials. This study aims to evaluate the impact computationally by performing optoelectronic simulations and optimizing the organic solar cell device.

Over the past decade, various multi-layer structures have been proposed and successfully integrated into tandem solar cell devices[12]. All-solution-processed multilayers are particularly appealing due to their compatibility with the printing techniques used in OSC fabrication. Additionally, a range of wide- and low-bandgap materials, particularly polymers, have been utilised as donor materials in tandem devices' front and rear sub-cells[13]. However, challenges such

*Corresponding author (E-mail: lahapinaki007@gmail.com)

as overlapping absorption spectra and low photovoltaic efficiency in single cells often limit the performance of tandem devices. Here, we report a tandem solar cell that employs the DPPEZnP-TBO layer as the electron donor material in both the front and rear sub-cells. DPPEZnP-TBO is a zinc porphyrin derivative designed for high-performance in bulk heterojunction (BHJ) organic solar cells. It combines a porphyrin core with donor–π–acceptor (D–π–A) structural ideas. DPPEZnP-TBO possesses a low bandgap and a broad absorption spectrum, making it suitable for harvesting near-infrared light. Its molecular structure allows for efficient charge transport and minimal energy losses, which are critical factors in achieving high PCEs in organic solar cells. These materials provide efficient and complementary absorption, enabling optimized devices to achieve a higher power conversion efficiency, setting a new benchmark for solution-processed organic solar cells. M. Li, *et al*. report a high-performance solution-processed tandem organic solar cell employing DPPEZnP-TBO as the electron donor material[14]. Current research is directed toward enhancing the properties of DPPEZnP-TBO and expanding its use across diverse solar cell architectures.

In this study, the Fluxim SETFOS software was employed to simulate the performance of DPPEZn P-TBO-based solar cells. This research investigated the impact of active layer thickness variations on the performance metrics of organic solar cells (OSCs). It further evaluates the effects of working temperature and series resistance on the overall performance of organic photovoltaic (OPV) devices, providing a comprehensive analysis to determine optimal operating conditions.

We employ PEDOT: PSS as an electrode and DPPEZnP-TBO as the active layer. Key performance parameters, including open-circuit voltage (V_{OC}), short-circuit current density (J_{SC}), fill factor (FF), and power conversion efficiency (PCE), are simulated to explore the impact of temperature, series resistance and active layer thickness on OSC efficiency. The device structure under investigation consists of layers arranged as ITO/PEDOT: PSS/DPPEZnP-TBO/ZnO/ PEDOT: PSS/DPPEZnP-TBO/Aluminium. The front electrode is formed by ITO and PEDOT: PSS, while the back electrode consists of aluminium (Al). Figure 1 illustrates the molecular structure of DPPEZnP-TBO[14].

2 Materials and Methods

2.1 Simulation methods

We used SETFOS, a commercial tool for simulating multilayer solar cells, to analyse the device. SETFOS is a robust tool for modelling the optical and electrical properties of organic devices, providing detailed insights into their performance and behaviour[15]. The SETFOS tool, developed by Fluxim, simulates organic tandem solar cells by solving macroscopic semiconductor transport equations and continuity equations for mobile and trapped electron and hole densities (n, p, n_t, p_t). The electrical behaviour of organic

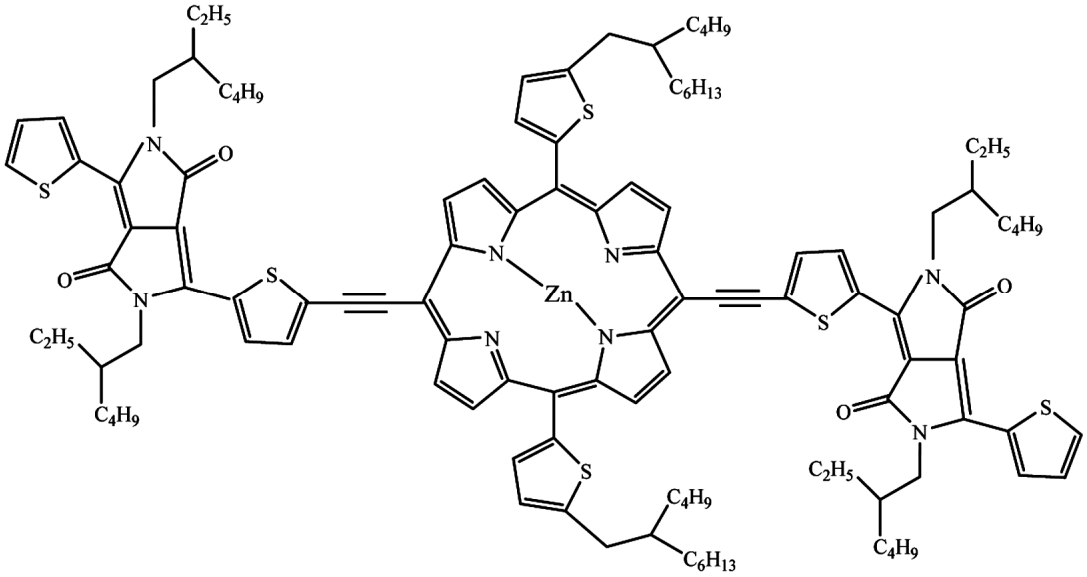

Fig. 1 — Molecular structure of DPPEZnP-TBO.

solar cells is described by drift-diffusion equations[16]. The drift-diffusion module calculates the current-voltage (J-V) characteristics, charge concentration, electric field, and recombination zone of photovoltaic devices by integrating drift-diffusion currents with Poisson's equation and a 1D light-propagation model for multi-layer structures[17].

The fundamental equations solved are the continuity equations for the densities of mobile and trapped electrons and holes, denoted n, p, n_t, and p_t, respectively[18].

$$\frac{\partial}{\partial t}n\,(z,t) = -\frac{1}{q}\frac{\partial}{\partial z}J_n(z,t) + \mathcal{G}\,(z,t) - \mathcal{R}_{nt}(z,t) - \mathcal{R}_{np}(z,t)\,, \quad \ldots (1)$$

$$\frac{\partial}{\partial t}p\,(z,t) = -\frac{1}{q}\frac{\partial}{\partial z}J_p(z,t) + \mathcal{G}\,(z,t) - \mathcal{R}_{pt}(z,t) - \mathcal{R}_{np}(z,t), \quad \ldots (2)$$

$$\frac{\partial}{\partial t}n_t\,(z,t) = \mathcal{R}_{nt_n}\,(z,t) - \mathcal{R}_{pt_n}\,(z,t) - \mathcal{R}_{t_nt_p}(z,t)\,, \quad \ldots (3)$$

$$\frac{\partial}{\partial t}p_t\,(z,t) = -\mathcal{R}_{nt_p}\,(z,t) + \mathcal{R}_{pt_p}\,(z,t) - \mathcal{R}_{t_nt_p}(z,t) \quad \ldots (4)$$

In these equations, t represents time, z is the transport direction, q denotes the elementary electronic charge, and $J_{n(p)}$ refers to the electron (hole) current density. The term G is the (optical) volume generation rate, while R_{np} describes the bi-molecular inter-band recombination rate.

The remaining rate terms account for various charge carrier trapping processes. The total electron (hole) trapping volume rate is expressed as $R_{nt} = R_{ntn} + R_{ntp}$ and $R_{pt} = R_{ptp} + R_{ptn}$. R_{nt} is the total electron trapping volume rate, and R_{pt} is the total hole trapping volume rate**.** Here, R_{ntn} represents electron capture by neutral traps, R_{ntp} electron capture by positively charged traps, R_{ptp} hole capture by positively charged traps**,** and R_{ptn} hole capture by neutral traps. $\mathcal{R}_{t_nt_p}$ denotes the trap–trap recombination rate between trapped electrons and trapped holes.

To simplify the model, excitons are not explicitly included, although their consideration is possible in SETFOS. Instead, photogeneration is expressed as G = A. η_{gen}, where A is the local absorption rate derived from the optical model, and η_{gen} is the generation efficiency. Recombination is limited to the Shockley-Read-Hall mechanism, neglecting bi-molecular and trap-trap terms. Only single defect levels near the mid-gap, treated as deep electron traps, are included[19]. For the currents in Eqns. (1) and (2), the standard drift-diffusion formulation is applied.

$$J_n\,(z,t) = q\mu_n\,(z,t)\left[n(z,t)\mathcal{E}\,(z,t) + \frac{k_BT}{q}\frac{\partial}{\partial t}n\,(z,t)\right] \quad \ldots (5)$$

$$J_p\,(z,t) = q\mu_p\,(z,t)\left[p(z,t)\mathcal{E}\,(z,t) + \frac{k_BT}{q}\frac{\partial}{\partial t}p\,(z,t)\right] \quad \ldots (6)$$

The Einstein relation is applied to substitute the diffusion constant with the charge carrier mobility μ, while the electric field Ɛ is determined from the solution of Poisson's equation.

$$\varepsilon_o\frac{\partial}{\partial t}[\varepsilon_r\,(z)\mathcal{E}\,(z,t)] = q[p\,(z,t) - n\,(z,t) + p_t\,(z,t) - n_t\,(z,t) + N_{don}(z) - N_{acc}(z)] \quad \ldots (7)$$

Here, ε_0 represents the vacuum permittivity, ε_r is the relative dielectric constant, and N_{acc} (N_{don}) denotes the density of ionized acceptor (donor) molecules. In organic semiconductors, the charge carrier mobilities in Eqns. (5) and (6) can also depend on the local electric field, often modelled using a Poole-Frenkel-type expression[20].

$$\mu_{pt} = \mu_{Dn,p}exp\left(\gamma_{n,p}\sqrt{|\mathcal{E}|}\right),\ \gamma_{n,p} = 1/\sqrt{\mathcal{E}_{0n,p^*}} \quad \ldots (8)$$

Finally, the charge carrier densities are described using Boltzmann occupation statistics, relating them to the effective density of states $N_{0n,\ p,}$ the HOMO/LUMO energies (accounting for the electrostatic potential profile), and the quasi-Fermi levels $EF_{n,p}$ as follows:

$$n\,(z,t) = N_{0n}\,(z)\,exp\left(\frac{EF_n(z,t) - LUMO\,(z,t)}{k_BT}\right) \quad \ldots (9)$$

$$p\,(z,t) = N_{0p}\,(z)\,exp\left(-\frac{EF_p(z,t) - HOMO\,(z,t)}{k_BT}\right) \quad \ldots (10)$$

This study focuses solely on the steady-state condition, where all time-dependent terms become negligible. Under these conditions, the trap-assisted inter-band recombination rate for a single defect level at energy E_t (measured from the conduction band minimum) with a density N_t is described using the Shockley-Read-Hall formalism[21].

$$\mathcal{R}_{nt}(z) = \mathcal{R}_{pt}(z) = \mathcal{R}_{SRH}(z) = \frac{[n\,(z)\,p\,(z) - n_i^2\,(z)]}{C_p^{-1}\,[n\,(z) + n_{t0}\,(z)\,] + C_p^{-1}\,[p\,(z) + p_{t0}\,(z)\,]} \quad \ldots (11)$$

Here, $C_{n,p}$ are the electron and hole capture rates,

$$n_{t0}\,(z) = N_{0n}\,(z)\,exp\left(\frac{E_t(z) - LUMO\,(z)}{k_BT}\right) \quad \ldots (12)$$

$$p_{t0}\,(z) = N_{0p}\,(z)\,exp\left(-\frac{E_t(z) - HOMO\,(z)}{k_BT}\right) \quad \ldots (13)$$

$$n_i^2\,(z) = N_{0n}\,(z)\,N_{0p}\,(z)\,exp\left(-\frac{E_g(z)}{k_BT}\right) \quad \ldots (14)$$

$$E_g(z) = LUMO\,(z) - HOMO\,(z) \quad \ldots (15)$$

By solving the steady-state drift-diffusion-Poisson equation problem and applying suitable boundary conditions for the charge carrier densities and the electric field. For the electric field calculation, the total potential drop across the device thickness L is defined as the difference between the applied voltage and the built-in potential.

$$\int_0^L dz\,\mathcal{E}\,(z) = V_{app} - V_{bi} \quad \ldots (16)$$

The built-in potential is derived from the work functions of the top and bottom electrodes, where $qV_{bi} = \Phi_{top} - \Phi_{bot}$. For the charge carrier densities, ohmic contacts are modelled using a Dirichlet boundary condition based on the electrode work functions, as expressed in equations (9) and (10). Thermionic injection is modelled according to Scott and Malliaras, where the injection currents are a (complex) function of carrier mobility, HOMO-LUMO levels, work function, effective density of states, dielectric constant, electric field, and temperature[22].

Here, the electrical simulations of tandem devices follow the hopping interface model, which describes charge transfer between the monolithically integrated sub-cells[23,24]. This model is based on Miller-Abrahams' theory of thermally activated hopping in disordered materials and defines individual rates for charge transfer in both intra- and inter-band transitions[25,26]. For tandem OPV simulations, only HOMO-LUMO transfer is considered, assuming an ideal junction concerning leakage currents. The rate of inter-band hopping, connecting the HOMO on the left side with the LUMO on the right side of the interface, is given by[24].

$$T_{lr}^{LH}\,(p_r) = a_r p_r \mathcal{V}\,exp\left(-\frac{|\Delta E_{l,r}| + \Delta E_{l,r}}{2k_BT}\right) \quad \ldots (17)$$

$$v = \nu \int dx \int dy\; exp[-\gamma d\,(x,y)] \quad \ldots (18)$$

In the expressions above, p_r and a_r denote the hole density and the molecular lattice spacing on the right-hand side, respectively. Here, ν is the attempt frequency of the hopping process (in units of $m^2\ s^{-1}$), and $d(x, y) = [(a_l + a_r)^2/4 + x^2 + y^2]^{1/2}$ is the hopping distance. γ is the inverse tunnelling distance, and $\Delta E_{l,r}$ is the energy difference between the left and right molecular states involved in the hopping process (Fig. 1). The following expression gives the tunnelling particle current density:

$$J_{lr}^{LH}\,(n_l, p_r) = a_l n_r T_{lr}^{LH}\,(p_r) \quad \ldots (19)$$

Here, n_l and a_l represent the electron density and molecular lattice spacing on the left side of the interface. Integration into the standard drift-diffusion-Poisson framework for classical continuum charge transport simulation is achieved by equating the tunnelling current with the drift-diffusion currents on both sides of the interface.

In this work, we use SETFOS to combine global and local optimisation algorithms to fit current-voltage (J-V) curves and extract material parameters, and to optimise layer thicknesses, operating temperature, and series resistance of tandem OPV devices for maximum performance. This optimization also focuses on maximising the minimum sub-cell photocurrents to achieve current matching. In optoelectronic optimization, the objective is to maximize the photovoltaic power conversion efficiency (PCE).

2.2 Device structures and material parameters

For the simulation of organic tandem solar cells, a high-efficiency device architecture is considered, comprising a DPPEZnP-TBO absorber and a recombination interlayer comprising a ZnO layer combined with PEDOT: PSS. The electrodes consist of PEDOT: PSS and Al. The device structure under investigation comprises multiple layers with specific functionalities. The transparent Indium Tin Oxide (ITO) layer allows light to enter the device. PEDOT: PSS acts as an electrode. The primary photoactive layer, DPPEZnP-TBO, absorbs light and generates excitons. The ZnO layer serves as the electron-transport layer, facilitating efficient electron extraction and transport. PEDOT: PSS is also used as a recombination layer, facilitating charge recombination within the tandem structure. The second photoactive layer, another DPPEZnP-TBO layer, further contributes to light absorption and exciton generation. Finally, luminium (Al) forms the reflective back electrode, collecting electrons and completing the circuit. ITO and PEDOT: PSS form the front electrode in this configuration, whereas aluminium serves as the back electrode. The layer structure and energy-level alignment of the experimental model used in the simulation are shown in Figs 2(a) and 2(b), respectively.

The optical material parameters (n vs k-data) and charge carrier mobilities were sourced from the literature[27].

3 Results and Discussion

The effects of various parameters on the cell's output are analysed to optimise the performance metrics of the proposed structure. The parameters examined include the thickness of the active layer, the impact of temperature variation and series resistance.

3.1 Effect of active layer thickness

Variation of Open Circuit Voltage (V_{OC}), Short Circuit Current Density (J_{SC}), Fill Factor (F.F.), and Power Conversion Efficiency (PCE) of OSCs with different active layer thicknesses is shown in Figs 3 (a-d), respectively.

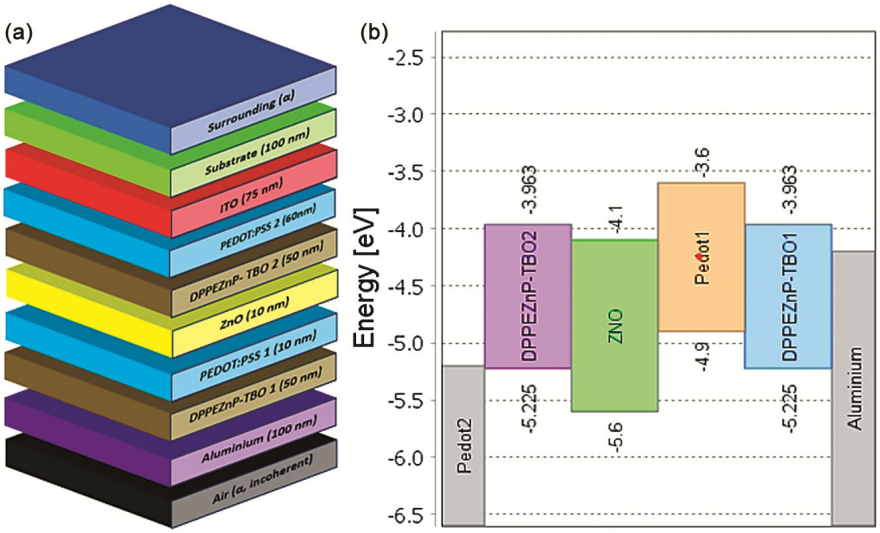

Fig. 2 — (a) Layer stack representing the organic cell structure and (b) Energy band alignment (before contact) of various layers in the OSC.

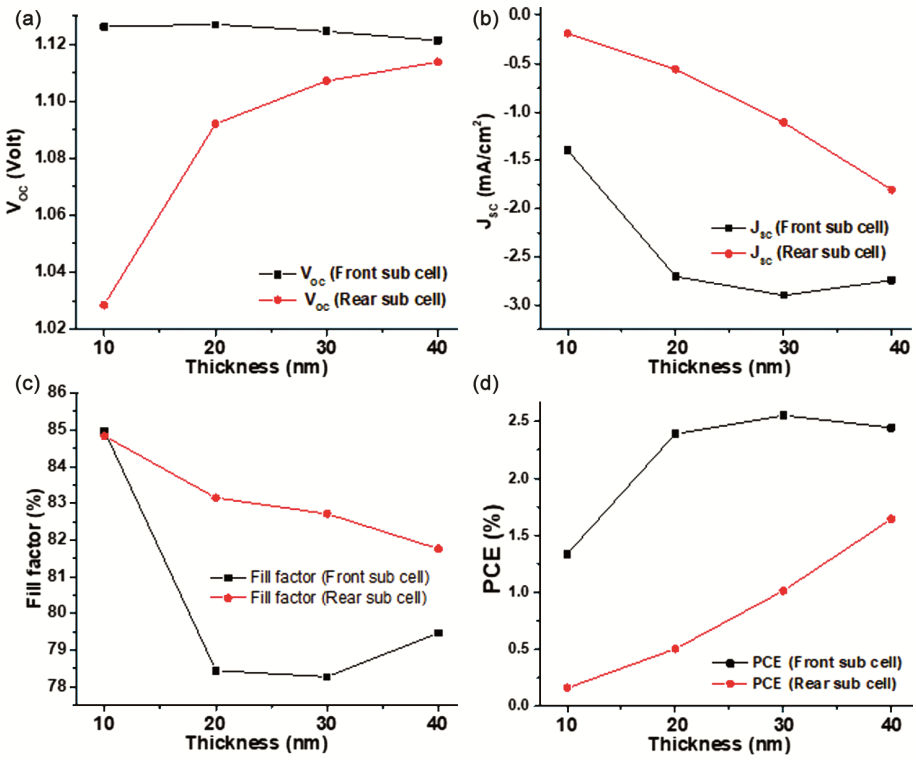

Fig. 3 — (a) Open circuit voltage (V_{OC}), (b) Short circuit current density (J_{SC}) (c) Fill factor (F.F.) and (d) Power conversion efficiency (PCE) of OSC with different active layer thickness.

To evaluate its impact on OSC performance, the active-layer thickness was varied from 10 nm to 40 nm for the front and rear sub-cells. The efficiency of the OSC depends primarily on four processes: photon absorption and exciton creation, exciton diffusion, charge transfer, and charge collection[28]. All these processes are strongly influenced by the thickness of the active layer (DPPEZnP-TBO). According to Beer-Lambert's law, absorption increases linearly with active layer thickness, meaning more photons are absorbed as the thickness increases. This enhanced photon absorption increases short-circuit current (J_{SC}) and power conversion efficiency (PCE), as shown in Figs 3(b) and 3(d), respectively. At an optimal thickness of 40 nm for the front sub-cell, J_{SC} and PCE reach 2.74 mA/cm² and 2.44%, respectively, whereas for the rear sub-cell, they are 1.80 mA/cm² and 1.64%, respectively. Although these output parameters show a slight increase beyond this thickness, the enhanced absorption is offset by increased recombination of free charge carriers in the active layer, as previously described[29].

$$E_{int} = \frac{V_{OC} \times V_{app}}{\tau} \quad \ldots (20)$$

In equation (20), E_{int} denotes the internal electric field, and V_{OC} and V_{app} denote the open-circuit voltage and the applied voltage, respectively. τ denotes the active-layer thickness. As the thickness increases, the electric field decreases, thereby reducing the carrier transport length and indirectly enhancing recombination. Equation (2) shows that V_{OC} is affected by both the dark generation current and the saturation current[30].

$$V_{OC} = \frac{nkT}{q} \ln\left(\frac{I_L}{I_0} - 1\right) \quad \ldots (21)$$

As thickness increases, the reverse saturation current decreases, thereby reducing the open-circuit voltage (V_{OC}), as illustrated in Fig. 3(a). The decrease in V_{OC} becomes less significant as the thickness increases for the front sub-cell. V_{OC} increases from 1.02 V to 1.11 V as the thickness increases from 10 nm to 40 nm, attributable to enhanced light absorption and improved charge generation at higher thicknesses, thereby increasing the overall potential.

The Short-Circuit Current Density (J_{SC}) varies significantly between the front and rear sub-cells. J_{SC} decreases with increasing thickness. This reduction is due to reduced charge-carrier diffusion and collection efficiency at higher thicknesses, leading to recombination losses.

The fill factor (FF) as a function of thickness is shown in Fig. 3 (c), where the sharp decline from 84.96 % to 79.47 % in the front sub-cell and for the rear sub-cell value decreases from 84.83 % to 81.75 % is attributed to the rise in series resistance with increasing layer thickness. This decline is attributed to the increase in series resistance caused by thicker active layers, which hinders efficient charge transport.

The maximum power conversion efficiency (%) value increases with thickness in front and rear sub-cells. The increase is primarily due to enhanced light absorption and better photon harvesting in thicker layers, compensating for losses in J_{SC} and FF.

3.2 Effect of temperature

The impact of working temperature on various cell parameters has been analysed, highlighting the sensitivity of organic solar cells to temperature variations, which is shown in Fig. 4. The temperature was varied between 275 K and 450 K.

Figure 4(a) illustrates the effect of temperature variations on the device's J-V curve. As the temperature increases, the open-circuit voltage (V_{OC}) decreases from 1.34 V to 0.57 V, as shown in Fig. 4(b). This reduction in V_{OC} is attributed to an increase in the reverse saturation current and increased charge recombination. The effect of temperature on short circuit current density

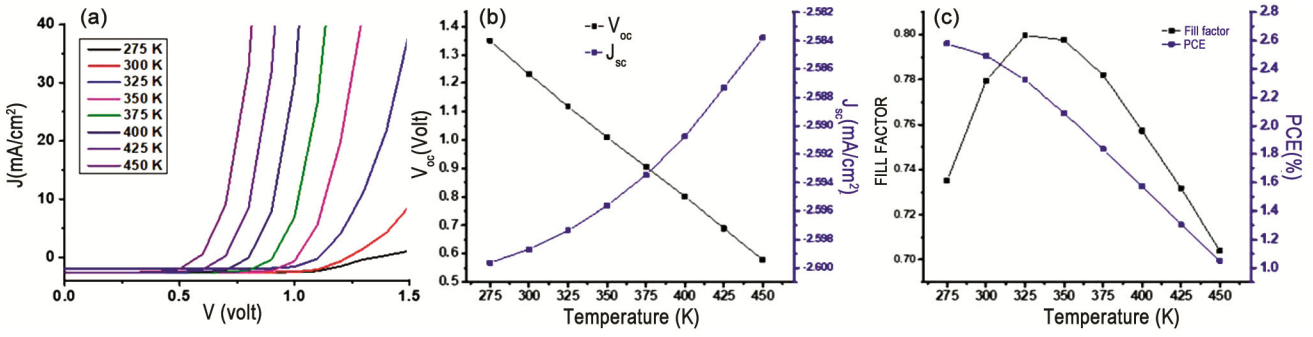

Fig. 4 — (a) Current (J) versus voltage (V) characteristics of OSC with different temperatures, (b) Open circuit voltage (V_{OC}) and (c) Fill factor (F.F.) and power conversion efficiency (PCE) of OSC with different temperatures..

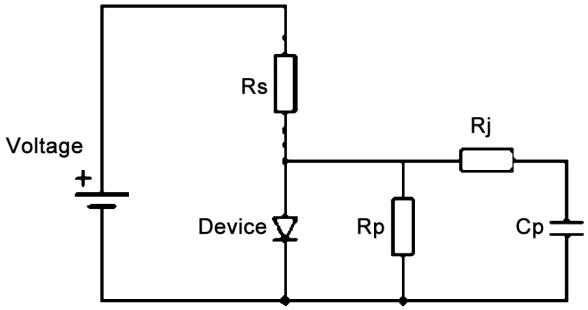

Fig. 5 — Solar cell equivalent circuit including series resistance and shunt resistance.

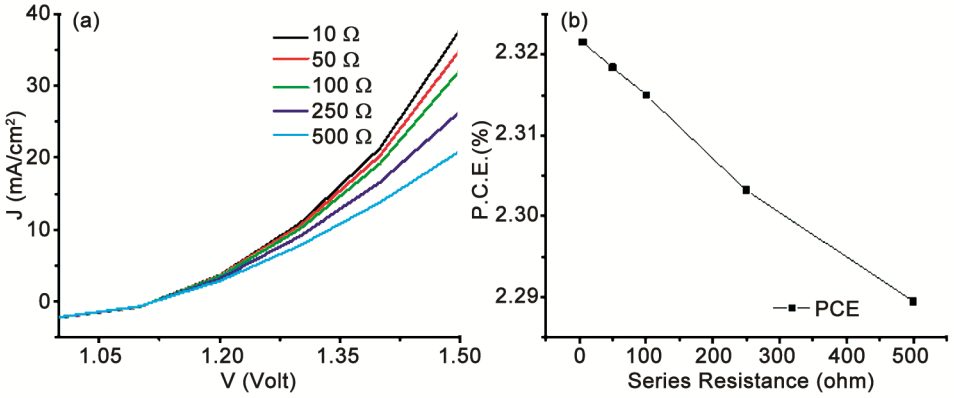

Fig. 6 — (a) Current (J) versus voltage (V) characteristics of OSC with different series resistance (R_S) and (b) Power conversion efficiency (PCE) of OSC with different series resistances.

(J_{SC}) is further clarified in Fig. 4(b). J_{SC} value increases from -2.59 mA/cm^2 to -2.58 mA/cm^2. J_{SC} value remains relatively constant with temperature due to the dominant effects of reduced V_{OC}. Additionally, the fill factor (FF) increases initially up to 325 K; thereafter, the FF value decreases linearly, as shown in Fig. 4(c). At below 325 K, thermal energy enhances the mobility of charge carriers within the active layers, leading to more efficient charge collection at the electrodes. This improved charge transport reduces resistive losses, thereby increasing FF. Moderate heating can reduce defects or energy barriers at the donor-acceptor interfaces, facilitating charge transfer and enhancing the FF[31]. Power conversion efficiency (PCE) decreases linearly, following a trend similar to that of V_{OC}, as shown in Fig. 4(c). The linear decrease in PCE in organic photovoltaic solar cells is primarily due to the temperature-induced drop in V_{OC}, caused by increased reverse saturation current and charge recombination. Additionally, a reduction in the fill factor (FF) at higher temperatures amplifies this decline, while J_{SC} remains nearly constant.

3.3 Effect of series resistance

Figure 5 illustrates the equivalent circuit of a solar cell, accounting for series (R_S) and shunt resistances (R_P). These resistances influence the cell's performance by affecting current flow and voltage output. Figure 6 (a) depicts the current-voltage (J-V) characteristics of an ITO/PEDOT: PSS/DPPEZnP-TBO/ZnO/PEDOT: PSS/ DPPEZnP-TBO/Aluminium organic solar cell under illumination. The J-V curve is significantly influenced by series resistance. Series resistance varies from 5 ohms to 500 ohms at 325 K. As shown in the figure, increasing the series resistance consistently reduces the current. This behaviour is due to the effect of series resistance on charge-carrier transport within the device. A higher series resistance results in a larger voltage drop across the device, thereby reducing the efficiency of current extraction. Consequently, the power conversion efficiency of the solar cell decreases with increasing series resistance, as shown in Fig. 6(b). PCE decreased from 2.32 % to 2.28%. Organic materials are particularly sensitive to such resistive losses because of their lower charge-carrier mobility than their inorganic counterparts. The increase in mobility enhances conductivity, thereby reducing the series resistance[29].

4 Conclusion

In conclusion, this study has analysed a simulated organic solar cell structure of ITO/PEDOT: PSS/DPPE-

ZnP-TBO/ZnO/PEDOT: PSS/DPPEZnP-TBO/Al to address key challenges in DPPEZnP-TBO–based devices. The results have shown that device optimization significantly improves key parameters such as power conversion efficiency (PCE), short-circuit current density (J_{SC}), open-circuit voltage (V_{OC}), and fill factor (FF). The effects of active-layer thickness, operating temperature, and series resistance have been examined to determine optimal conditions. At 325 K, the device has exhibited a V_{OC} of 1.11 V, J_{SC} of −2.59 mA/cm², FF of 79%, and PCE of 2.32%. With a 40 nm front sub-cell active layer, V_{OC} has increased to 1.12 V and PCE to 2.44%, while FF has remained 79%. With a series resistance of 500 Ω, the device has maintained a V_{OC} of 1.12 V, J_{SC} of −2.59 mA/cm², FF of 79%, and PCE of 2.28%.

These findings provide useful insights for improving the efficiency of DPPEZnP-TBO-based organic solar cells and support the development of high-performance organic photovoltaic devices.

Acknowledgement

The authors gratefully acknowledge L.N.D. College, Motihari, a constituent unit of B.R.A. Bihar University, Muzaffarpur, for providing access to the simulation software FLUXIM-SETFOS (version 5.5).

References

1 Li Y, *Acc Chem Res*, 45 (2012) 723.
2 Li G, Zhu R & Yang Y, *Nat Photonics*, 6 (2012) 153.
3 Espinosa N, Høsel M, Angmo D & Krebs F C, *Energy Environ Sci*, 5 (2012) 5117.
4 Zhu L, Zhang M, Zhou Z *et al.*, *Nat Rev Electr Eng*, 1 (2024) 581.
5 Choi H, Ryu S U, Lee D H, Kim H, Song S, Kim H I & Park T, *ACS Energy Lett*, 9 (2024) 3136.
6 Khosroabadi S, Eghbali R & Shokouhmand A, *J Mater Sci Mater Eng*, 19 (2024) 28.
7 Ecker B, Posdorfer J & von Hauff E, *Sol Energy Mater Sol Cells*, 116 (2013) 176.
8 Anrango-Camacho C, Pavón-Ipiales K, Frontana-Uribe B A & Palma-Cando A, *Nanomaterials*, 12 (2022) 443.
9 Barman S N & Laha P, *Mater Sci Res India*, 22 (2026) 183.
10 Jia Z, Qin S, Meng L *et al.*, *Nat Commun*, 12 (2021) 178.
11 Liang X, Wang J, Miao R, Zhao Q, Huang L, Wen S & Tang J, *Dyes Pigments*, 198 (2022) 109963.
12 Dharmadasa I M, *Sol Energy Mater Sol Cells*, 85 (2005) 293.
13 Ko S J, Choi H, Hoang Q V, Song C E *et al.*, *Carbon Energy*, 2 (2020) 131.
14 Li M, Gao K, Wan X *et al.*, *Nat Photonics*, 11 (2017) 85.
15 *Semiconducting Thin Film Optics Simulator (SETFOS)*, Version 5.2, Fluxim AG (Switzerland), 2022.
16 Zojer K, *Adv Opt Mater*, 9 (2021) 2100219.
17 Lin A S & Phillips J D, *IEEE Trans Electron Devices*, 56 (2009) 3168.
18 Aeberhard U, Schiller A, Masson Y *et al.*, *Front Photonics*, 3 (2022).
19 Ryu S, Ha N Y, Ahn Y H *et al.*, *Sci Rep*, 11 (2021) 16781.
20 Frenkel J, *Phys Rev*, 54 (1938) 647.
21 Shockley W & Read W T, *Phys Rev*, 87 (1952) 835.
22 Scott J C & Malliaras G G, *Chem Phys Lett*, 299 (1999) 115.
23 Altazin S, Kirsch C, Knapp E, Stous A & Ruhstaller B, *J Appl Phys*, 124 (2018) 135501.
24 Altazin S, Stepanova L, Werner J, Niesen B, Ballif C & Ruhstaller B, *Opt Express*, 26 (2018) A579.
25 Miller A & Abrahams E, *Phys Rev*, 120 (1960) 745.
26 Coropceanu V, Cornil J, da Silva Filho D A, Olivier Y, Silbey R & Brédas J L, *Chem Rev*, 107 (2007) 926.
27 Xiao J, Zhao M, Wang Y & Zhang X, *Nanophotonics*, 6 (2017) 1309.
28 Xie Y & Wu H, *Mater Today Adv*, 5 (2020) 100048.
29 Mir A M, Bashir F, Khanday F A, Zahoor F, Hanif M & May Z, *IEEE Access*, 12 (2024) 10961.
30 Abdelaziz W, Shaker A, Abouelatta M & Zekry A, *Opt Mater*, 91 (2019) 239.
31 Ouslimane T, Et-taya L, Elmaimouni L & Benami A, *Heliyon*, 7 (2021) e06379.